

Multi-species optically addressable spin defects in a van der Waals material

Received: 27 June 2024

Accepted: 29 July 2024

Published online: 07 August 2024

Check for updates

Sam C. Scholten ^{1,2,3,10}, Priya Singh ^{1,10}, Alexander J. Healey¹,
Islay O. Robertson ¹, Galya Haim^{2,4}, Cheng Tan¹, David A. Broadway ¹,
Lan Wang ^{1,5}, Hiroshi Abe ⁶, Takeshi Ohshima ^{6,7}, Mehran Kianinia ^{8,9},
Philipp Reineck ¹, Igor Aharonovich ^{8,9} ✉ & Jean-Philippe Tetienne ¹ ✉

Optically addressable spin defects hosted in two-dimensional van der Waals materials represent a new frontier for quantum technologies, promising to lead to a new class of ultrathin quantum sensors and simulators. Recently, hexagonal boron nitride (hBN) has been shown to host several types of optically addressable spin defects, thus offering a unique opportunity to simultaneously address and utilise various spin species in a single material. Here we demonstrate an interplay between two separate spin species within a single hBN crystal, namely $S = 1$ boron vacancy defects and carbon-related electron spins. We reveal the $S = 1/2$ character of the carbon-related defect and further demonstrate room temperature coherent control and optical readout of both $S = 1$ and $S = 1/2$ spin species. By tuning the two spin ensembles into resonance with each other, we observe cross-relaxation indicating strong inter-species dipolar coupling. We then demonstrate magnetic imaging using the $S = 1/2$ defects and leverage their lack of intrinsic quantization axis to probe the magnetic anisotropy of a test sample. Our results establish hBN as a versatile platform for quantum technologies in a van der Waals host at room temperature.

Hexagonal boron nitride (hBN) has come to prominence as a host material for optically addressable spin defects for quantum technology applications^{1–4}. The layered van der Waals structure of hBN makes it particularly appealing for nanoscale quantum sensing and imaging, as the spin defects can in principle be confined within hBN flakes just a few atoms thick³. The prospect of two-dimensional (2D) confinement of a dipolar spin system is also attractive for quantum simulations, as it would open the door to realising exotic ground-state phases such as

spin liquids^{6,7} as well as exploring many-body localisation and thermalisation in 2D^{8–12}. To date, only the negatively charged boron vacancy (V_{B}^{-}) defect has been used for such quantum applications¹. The V_{B}^{-} defect is a ground-state spin triplet ($S = 1$) with a quantisation axis along the c -axis of the hBN crystal and a zero-field splitting of $D \approx 3.45$ GHz between the $m_S = 0$ and $m_S = \pm 1$ spin sublevels. Owing to a spin-dependent intersystem crossing, the electronic spin transitions of the V_{B}^{-} defect, i.e. $|0\rangle \leftrightarrow |\pm 1\rangle$, can be probed via optically detected

¹School of Science, RMIT University, Melbourne VIC 3001, Australia. ²School of Physics, University of Melbourne, Melbourne VIC 3010, Australia. ³Centre for Quantum Computation and Communication Technology, School of Physics, University of Melbourne, Melbourne VIC 3010, Australia. ⁴Department of Applied Physics, The Hebrew University of Jerusalem, Safra Campus, Givat Ram Jerusalem 91904, Israel. ⁵Low Dimensional Magnetism and Spintronic Devices Lab, School of Physics, Hefei University of Technology, 230009 Hefei, Anhui, China. ⁶National Institutes for Quantum Science and Technology (QST), 1233 Watanuki, Takasaki Gunma 370-1292, Japan. ⁷Department of Materials Science, Tohoku University, 6-6-02 Aramaki-Aza, Aoba-ku Sendai 980-8579, Japan. ⁸School of Mathematical and Physical Sciences, University of Technology Sydney, Ultimo NSW 2007, Australia. ⁹ARC Centre of Excellence for Transformative Meta-Optical Systems, Faculty of Science, University of Technology Sydney, Ultimo NSW 2007, Australia. ¹⁰These authors contributed equally: Sam C. Scholten, Priya Singh. ✉ e-mail: igor.aharonovich@uts.edu.au; jean-philippe.tetienne@rmit.edu.au

magnetic resonance (ODMR). The sensitivity of these transitions to the defect's environment in turn enables accurate measurements of magnetic fields, temperature and strain, as well as spatial imaging of these fields^{13–20}.

Meanwhile, several groups have reported the observation of a family of hBN defects emitting primarily at visible wavelengths and exhibiting ODMR with no apparent (or very weak) zero-field splitting^{21–25} akin to an effective spin doublet ($S = 1/2$). The exact structure of these defects as well as their spin multiplicity remain unknown, although they are generally believed to be related to carbon impurities^{21,26–29}. The deterministic creation of these spin defects is also an ongoing challenge^{3,21,25} and consequently, these $S = 1/2$ -like defects have not been exploited in sensing applications despite the unique possibilities afforded by the lack of intrinsic quantisation axis. More generally, having multiple optically addressable spin systems within a single layered solid would open new opportunities for quantum technologies. In this Article, we demonstrate the co-existence of two distinct optically addressable spin species in hBN.

Results

The two spin defects at the heart of this work are represented in Fig. 1a. The first is the V_B^- defect, which emits in the near-infrared¹. The second spin species is the carbon-related defect emitting in the visible, which we will refer to as $C_?$ —a proposed candidate is the carbon trimer C_2C_N ^{28,29}. We found that these $C_?$ spin defects are present in a variety of hBN samples both commercially sourced (powders and bulk crystals) and lab-grown by metal-organic vapour-phase epitaxy (MOVPE), see Table 1. In the following, we leverage the unique characteristics of each sample to demonstrate the isotropic character of the $C_?$ defects (using hBN powder), explore the interplay between V_B^- and $C_?$ spins (using a bulk crystal), and demonstrate quantum sensing using the $C_?$ defect (using a thin MOVPE film).

Co-existence of V_B^- and $C_?$

We first consider a commercially sourced hBN powder (see Table 1 and Supplementary Figs. 2–5). The photoluminescence (PL) spectrum of the as-received powder under laser excitation ($\lambda = 532$ nm wavelength) shows visible PL emission characteristic of the $C_?$ defect²¹, mainly centred around $\lambda = 550$ – 650 nm with a tail extending in the near-infrared up to 900 nm [Fig. 1b]. To create V_B^- defects, the as-received powder was irradiated with high-energy electrons, causing the appearance of a broad near-infrared emission peak centred around 820 nm characteristic¹ of the V_B^- defect [Fig. 1b].

Next, we used radiofrequency (RF) fields to probe the spin transitions of the defects via spin-dependent PL. A continuous-wave (CW) ODMR spectrum of the $S = 1$ V_B^- defect ensemble is obtained by collecting the V_B^- emission (750 – 1000 nm) as a function of RF frequency [Fig. 1c]. Under zero magnetic field ($B_0 = 0$), a single resonance at $f_r = D \approx 3.45$ GHz is observed corresponding to the nearly degenerate electronic spin transitions $|0\rangle \leftrightarrow |\pm 1\rangle$ [see energy level diagram in Fig. 1d]. Upon applying a magnetic field, this central resonance splits into two broad resonances due to the Zeeman effect, where the significant broadening is the result of the random orientation of the defects in the powder, as shown in the resonance frequencies calculated for a range of orientations [Fig. 1d].

On the other hand, the ODMR spectrum of the $C_?$ defects (550 – 700 nm) shows a single resonance at a frequency f_r that scales linearly with the applied field B_0 [Fig. 1e], thus resembling a $S = 1/2$ electronic system. Fitting the data with $hf_r = g_C \mu_B B_0$ where h is Planck's constant and μ_B the Bohr magneton, yields a g -factor of $g_C = 2.0(1)$ [Fig. 1f]. The powdered nature of the sample and the relatively large orientation-averaged ODMR contrast (of about -1%) provide a strong indication that the mechanism underpinning ODMR is intrinsically isotropic, i.e. independent of the direction of the applied field relative to the crystal orientation, rather than relying on an intersystem crossing in a $S \geq 1$ spin system as was suggested previously²³.

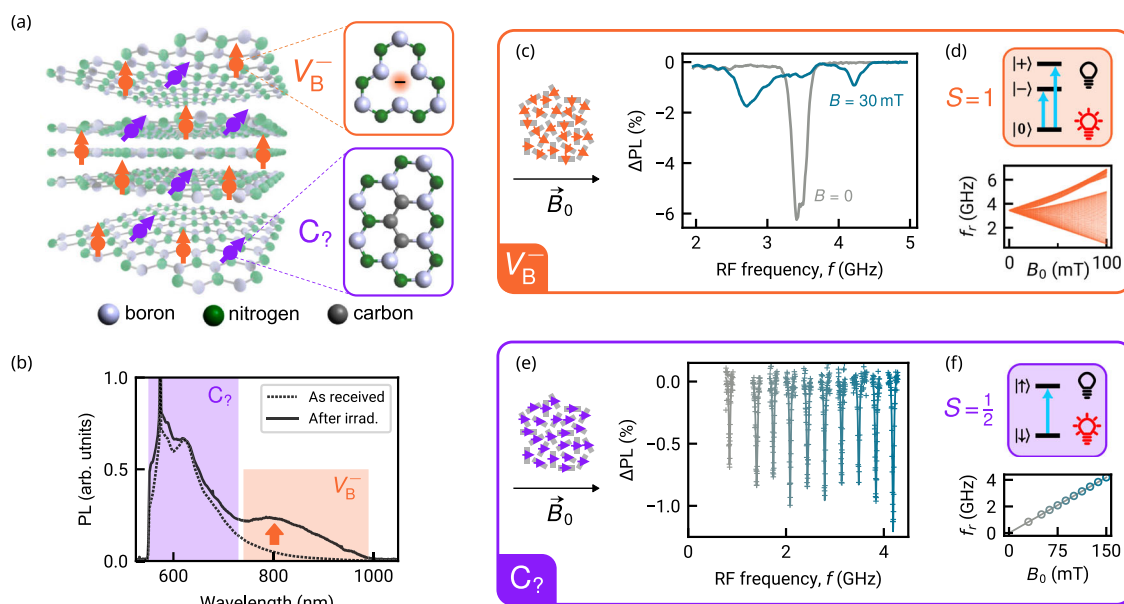


Fig. 1 | Multiple optically addressable spin defects in hBN. **a** Schematic representation of two co-existing species of spin defects in hBN: the boron vacancy defect (V_B^- , orange arrows) and a carbon-related defect (referred to as $C_?$, purple arrows). An example candidate for $C_?$ is shown, namely the C_2C_N defect.

b Photoluminescence (PL) spectra of hBN powder as received (dotted line) and after electron irradiation (solid line), under $\lambda = 532$ nm laser excitation. The shaded areas indicate the main emission band of $C_?$ (present in the as-received powder) and V_B^- (created by irradiation). **c** Optically detected magnetic resonance (ODMR) spectra of the V_B^- defects (PL band 750 – 1000 nm) in hBN powder at $B_0 = 0$ (grey

line) and $B_0 = 30$ mT (blue). **d** Energy level diagram of the V_B^- spin triplet. The spin eigenstates are denoted as $|0, \pm\rangle$ in the general case of an arbitrarily oriented magnetic field. The graph shows the calculated spin resonance frequencies f_r as a function of B_0 for a range of field orientations. **e** ODMR spectra of the $C_?$ defects (PL band 550 – 700 nm) in the same hBN powder as in (c), at different field strengths B_0 from 30 mT to 150 mT (left to right). **f** Energy level diagram of the $C_?$ effective spin doublet. The graph shows the spin resonance frequency f_r inferred from (e) as a function of B_0 (dots). The solid line is a linear fit, indicating a g -factor of $2.0(1)$.

Table 1 | Summary of the hBN samples used in this work

Sample description	Irradiation	Presence of C ₂ defects	Max. ODMR contrast	Sample morphology for measurements
Nanopowder (Graphene Supermarket)	2 MeV electrons	High density as purchased	-1.0% (batch 1)	powder film, ~1–10 μm thick (Fig. 1)
			+1.0% (batch 2)	powder film, ~1–10 μm thick (Supplementary Fig. 19)
Bulk crystal (HQ Graphene)	2 MeV electrons	Low density as purchased, high density after irradiation	+0.5%	whole crystal, ~100 μm thick (Fig. 3)
				exfoliated flake, ~1 μm thick (Fig. 2)
MOVPE film ²¹	none	High density as grown	+0.5%	film, ~40 nm thick (Fig. 4)

Column 3 indicates the qualitative density of C₂ defects (low/high density means single emitters can/cannot be resolved). Column 4: Maximum CW-ODMR contrast observed for the C₂ defects.

Spin multiplicity of the C₂ defect

To gain further insights into the nature of the C₂ spin defect and the origin of the ODMR contrast, we now use a flake exfoliated from a bulk electron-irradiated hBN crystal (see Table 1 and Supplementary Figs. 6, 7, here the ODMR contrast is about +0.5%). The single crystal orientation allows us to align the magnetic field with the V_B⁻ spin's quantisation axis and drive a single spin transition, e.g. |0⟩ → |-1⟩ [Fig. 2a], whose coherent dynamics can then be precisely compared to that of the C₂ spins. First, we perform a Rabi experiment whereby each spin ensemble is driven by a resonant RF pulse of variable duration and the corresponding PL monitored [Fig. 2b]. Rabi oscillations are observed both for the V_B⁻ ensemble [Fig. 2c] and the C₂ ensemble [Fig. 2d], demonstrating coherent control and optical readout of two distinct spin species within the same host material, at room temperature.

We can now address the question of the spin multiplicity of the C₂ defect, making use of the fact that the Rabi flopping frequency (Ω_C) directly depends on the spin quantum number (S) of the driven species according to $h\Omega_C = f(S)g_C\mu_B B_1$ where B₁ is the magnitude of the driving field and f(S) is a dimensionless function of S. To calibrate B₁, we measure the Rabi frequency of the S = 1 V_B⁻ ensemble, which is given by $h\Omega_V = g_V\mu_B B_1/\sqrt{2}$ where $g_V = 2.00 \approx g_C$ is the V_B⁻ g-factor¹, and compare it to Ω_C, measured at the same resonance frequency f_r [Fig. 2a] to ensure B₁ is identical in both Rabi measurements. We find that Ω_C is consistently smaller than Ω_V, with a ratio $\Omega_C/\Omega_V \approx 1/\sqrt{2}$ that reveals the S = 1/2 character of the C₂ defect's magnetic resonance [Fig. 2e]. Consequently, we can rule out a pure S = 1 or S = 3/2 system, which would give $\Omega_C/\Omega_V = \sqrt{2}$ (blue box, see Supplementary Note 5 A for a detailed discussion).

Rather than a single S = 1/2 system, which is not normally expected to give rise to ODMR, we propose a more specific interpretation whereby the C₂ defect would instead involve a pair of weakly coupled S = 1/2 particles (e.g. two unpaired electrons). Such a system also satisfies $\Omega_C/\Omega_V = 1/\sqrt{2}$ ³⁰, while providing a more natural explanation for the ODMR contrast by invoking different photon absorption/emission probabilities for the singlet and triplet configurations of the spin pair^{31–33}. In this scenario, the optical readout would distinguish the parallel spin states (pure triplet states |↑↑⟩ and |↓↓⟩) from the anti-parallel states (singlet-triplet mixtures of |↑↓⟩ and |↓↑⟩). We provide evidence supporting the spin pair theory in Supplementary Note 5E and Supplementary Fig. 12.

Cross-relaxation between V_B⁻ and C₂

So far we have used the V_B⁻ and C₂ spin ensembles independently. We now study the dynamics and interplay between the two spin species. To this end, we use again a single-crystal hBN sample containing both V_B⁻ and C₂ spins, and apply a magnetic field to tune the |0⟩ ↔ |-1⟩ transition of the V_B⁻ spins in resonance with the |↑⟩ ↔ |↓⟩ transition of the C₂ spins [Fig. 3a], here |↑⟩ and |↓⟩ refer to the states of either of the spin pair partners]. At the resonant field of $B_0 = hD/[(g_C + g_V)$

$\mu_B] \approx 62$ mT, the two spin ensembles can exchange energy causing an increased relaxation of their respective spin populations [Fig. 3a], a process known as cross-relaxation (CR)^{34,35}.

To probe the CR resonance, we use a fixed free interaction time τ between the initial laser pulse (which partially polarises both spin species) and the probe RF pulse [Fig. 3b], while varying the field strength B₀. For each value of B₀, the RF frequency of the probe pulse is scanned to construct a pulsed ODMR spectrum [Fig. 3c, d] and extract a normalised spin contrast [plot against B₀ in Fig. 3e]. This spin contrast is a measure of the amount of spin polarisation averaged over the sequence, which depends on the CR coupling present during the free interaction time τ as well as during the laser pulse where CR competes with optically induced spin polarisation. Examining the V_B⁻ spin contrast first, we see that the V_B⁻ ensemble experiences a reduced spin polarisation at the CR resonance [Fig. 3c], indicating coupling with a bath of S = 1/2 electron spins, which includes the C₂ defects^{36,37}. Crucially, the C₂ defects also exhibit a reduced spin polarisation at the CR resonance [Fig. 3d], providing unambiguous evidence of C₂ -V_B⁻ coupling.

We model the CR effect by considering the coupling of each spin to its nearest neighbour from the opposite spin species (see details in Supplementary Note 6B and Supplementary Fig. 14). For simplicity we assume the system to be initialised into the interacting state. We note that changing the initialisation using a combination of fast magnetic field control and RF pulses³⁸ could in principle reveal the direction of spin polarisation of the C₂ defect. For the C₂ spins, the mean distance to the nearest V_B⁻ is approximately 5 nm based on the estimated density of $[V_B^-] = 10^{18}$ cm⁻³. The resulting model with no free parameter [purple line in Fig. 3(e)] is in good agreement with the data, confirming that we do indeed detect CR between the C₂ and V_B⁻ spin ensembles. For the V_B⁻ case, we leave the total density of S = 1/2 spins free; best fit to the data is obtained for $[S = 1/2] = 5 \times 10^{18}$ cm⁻³ corresponding to a mean distance between nearest neighbours of approximately 3 nm. This cross-relaxation experiment thus reveals the high density of S = 1/2 spins in this hBN sample, and could be applied to determine the spin content of hBN flakes subject to various treatments. More generally, the demonstrated coupling between two optically addressable spin species of different multiplicities could be a useful new resource for future quantum technologies.

Magnetic imaging with the C₂ defect

Having established the S = 1/2 character of the C₂ defect, we now explore its potential for quantum sensing and imaging. The key advantage of the C₂ spin is its lack of intrinsic quantisation axis, allowing magnetometry to be performed under any direction of the external magnetic field. This feature is in contrast to spin defects with uniaxial anisotropy such as the V_B⁻ defect or the nitrogen-vacancy centre in diamond which are restricted to a narrow range of field directions and magnitudes due to spin mixing caused by transverse fields³⁹.

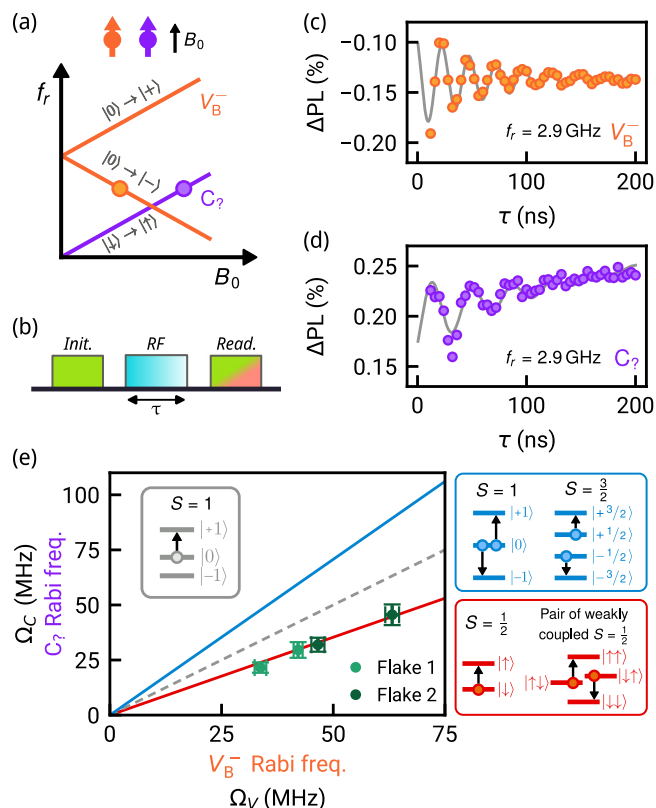


Fig. 2 | Coherent spin control at room temperature and $S = 1/2$ character of the C_2 defect. **a** Diagram depicting the spin resonance frequencies f_r of the V_B^- and C_2 defects as a function of the magnetic field strength B_0 applied parallel to the c -axis of the hBN crystal. **b** Pulse sequence used for the Rabi measurement. **c, d** Rabi oscillations of (c) the V_B^- defects at $B_0 = 20$ mT and of (d) the C_2 defects at $B_0 = 100$ mT in an exfoliated single-crystal hBN flake. The resonance frequency being driven is $f_r = 2.9$ GHz in both cases [see circles in (a)]. **e** Rabi frequency of the C_2 defects (Ω_C) as a function of the Rabi frequency of the V_B^- defects (Ω_V). Measurements taken from two different flakes are shown, see raw data in Supplementary Fig. 9. The error bars correspond to one standard error in the Rabi fit, see details in Supplementary Note 5B and Supplementary Figs. 10, 11. The solid lines correspond to the expectation under different assumptions for the spin multiplicity of the C_2 defects: a single $S = 1/2$ or a pair of weakly coupled $S = 1/2$ particles (red line); a pure $S = 1$ or $S = 3/2$ system with negligible zero-field splitting (blue line). The dashed line is the $\Omega_C = \Omega_V$ reference corresponding to driving a single transition of a $S = 1$ system.

To demonstrate magnetic imaging, we used a 40-nm-thick hBN film grown by MOVPE with precursors tuned to create a dense and uniform ensemble of C_2 spin defects^{21,40} (see Table 1 and Supplementary Fig. 8). Importantly, large flakes (hundreds of micrometres laterally) of the continuous wafer-scale film can be transferred from the growth substrate to the target sample [Fig. 4a and Supplementary Fig. 15] while preserving a uniform, well-defined thickness, an advantage over exfoliation from a bulk hBN crystal.

As a test magnetic sample, we used micron-sized flakes of Fe_3GaTe_2 , a ferromagnetic van der Waals material with a Curie temperature just above room temperature and a perpendicular magnetic anisotropy⁴¹. A single piece of the hBN film enables us to cover a multitude of Fe_3GaTe_2 flakes [Fig. 4b] which can then be magnetically imaged by performing widefield ODMR measurements of the C_2 defects. ODMR spectra on and off the magnetic flakes reveal local Zeeman shifts of up to $\Delta f_r \approx 100$ MHz [Fig. 4c], corresponding to stray fields $\Delta B = h\Delta f_r/g_C\mu_B \approx 3$ mT. Since the magnitude of the applied field is $B_0 \approx 35$ mT $\gg \Delta B$, the measured sample's stray field ΔB corresponds to the projection along the direction of \vec{B}_0 .

By fitting the ODMR spectrum at each pixel of the image, we can construct a ΔB map of a Fe_3GaTe_2 flake, for example in Fig. 4d where \vec{B}_0 is along the easy axis of magnetisation ($\theta_B = 0^\circ$). The flake appears uniformly magnetised, as confirmed by the good agreement with the simulation [Fig. 4e] which assumed a uniform out-of-plane magnetisation of $M_s = 160$ kA/m, in line with the expected value at room temperature⁴¹. A more detailed magnetisation map of the flake can be reconstructed from the data through a reverse propagation method [Supplementary Fig. 18]. A line cut across the flake [Fig. 4f] indicates a spatial resolution of about 600 nm in good agreement with the diffraction limit of our setup, which could be improved to 300 nm using a higher numerical-aperture objective.

As \vec{B}_0 is rotated away from the easy axis, the stray field becomes weaker overall [Fig. 4g, h] and nearly vanishes in the purely in-plane case ($\theta_B = 90^\circ$). This indicates the formation of multiple domains of opposite signs within the flake in the absence of a stabilising out-of-plane field, consistent with the findings in ref. 41. Note that the pattern of the residual stray field at $\theta_B = 90^\circ$ suggests the remanent magnetisation still points along the easy axis (see Supplementary Fig. 17), confirming the strong out-of-plane anisotropy of the material. Angle-dependent images of additional flakes are shown in Supplementary Fig. 16.

These measurements illustrate the utility of the isotropic C_2 defect to study micron-sized magnetic samples. The omnidirectional magnetometry allows the application of magnetic fields along arbitrary easy or hard axes and spanning a broad range of magnitudes from about 10 mT (below which the ODMR contrast drops) up to 300 mT or more (only limited by the RF electronics), allowing the precise determination of unknown anisotropies. As an example, it could be applied to test the potential existence of easy axes within in-plane ferromagnets such as monolayer $CrCl_3$, which is believed to exhibit 2D-XY ferromagnetism⁴² but has not been systematically investigated as a function of the azimuthal angle of \vec{B}_0 . Such measurements are generally inaccessible or impractical with current stray field techniques.

The shot-noise-limited magnetic sensitivity of our 40-nm-thick MOVPE film is about $100 \mu T/\sqrt{Hz}$ per $(500 \text{ nm})^2$ pixel (see Supplementary Note 7E), which is an order of magnitude better than that obtained with V_B^- defects in flakes of similar thickness^{15,16} thanks to the higher brightness of the C_2 defects. Crucially, this sensitivity is already sufficient to image atomically thin ferromagnets and investigate the emerging field of Moiré magnetism⁴³, for example, and could be boosted by using advanced sensing protocols^{44,45} and potentially by optimising sample fabrication.

Besides the unique omnidirectional magnetometry capability and the relative ease of fabrication compared to existing quantum sensing platforms like diamond, another advantage of the hBN platform is the possibility of leveraging the multiple spin species available. In particular, the C_2 defect is an ideal complement to V_B^- -based temperature and strain sensing¹³ as it is insensitive to variations in those quantities (an expected consequence of its $S = 1/2$ character and negligible orbital magnetic moment), and remains a reliable magnetometer regardless of sensor geometry (for instance in the presence of flake rippling or powder averaging). In this sense, a co-present C_2 ensemble can be viewed as augmenting a V_B^- ensemble tasked with temperature and strain sensing, with orientation-independent magnetic sensitivity. We envisage that this dual-spin multi-modal imaging capability will present new opportunities for studying phase transitions where the magnetic properties of a sample can be spatially correlated with the temperature profile or mechanical properties of a sample, and illustrate this capability with a proof-of-principle experiment, see Supplementary Figs. 19, 20.

More generally, the co-existence of two distinct spin ensembles within a single host material, which can both be optically initialised, read out, and coherently driven, at room temperature, distinguishes hBN from established material platforms such as diamond and silicon

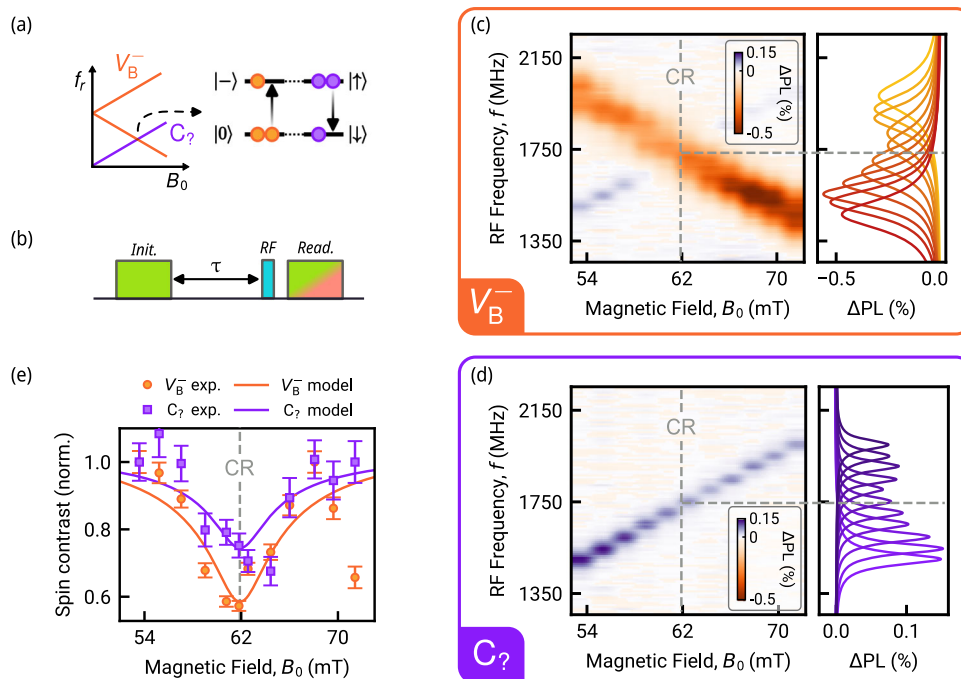


Fig. 3 | Cross-relaxation between two optically addressable spin species.

a Diagram illustrating the cross-relaxation (CR) resonance condition between the V_B^- and C_7 spin ensembles, at which the ensembles exchange energy. The populations (circles) are for illustrative purpose only, as the sign and level of spin polarisation of the C_7 spins is unknown. **b** Schematic of the pulsed ODMR sequence, which includes an interaction time $\tau = 350$ ns before applying the RF pulse. **c, d** Pulsed ODMR spectra as a function of B_0 for the V_B^- (**c**) and C_7 (**d**) defects near

the CR resonance. Lorentzian fits to the individual ODMR spectra are plotted together on the right with different colours for the different values of B_0 . The corresponding raw data is shown in Supplementary Fig. 13. **e** Spin contrast of each spin ensemble as a function of B_0 , corresponding to the ODMR contrast extracted from (**c, d**) after a linear slope was subtracted to remove RF power variations across the frequency range, normalised to 1 away from the CR resonance. The solid lines are the result of a model of the CR effect, see main text.

carbide in which only one type of optically addressable spin defect can generally be stabilised in a given sample⁴⁶. Combined with the prospect of 2D confinement afforded by the layered structure of hBN, which appears realistic given the recent observation of V_B^- defects in few-layer hBN⁵, hBN emerges as a rich and promising platform for future quantum technologies.

Methods

Experimental setup

The experiments reported in this work were carried out on a custom-built wide-field fluorescence microscope. The typical experimental setup and conditions are indicated below.

Optical excitation from a continuous-wave (CW) $\lambda = 532$ nm laser (Laser Quantum Opus 2 W) was gated using an acousto-optic modulator (Gooch & Housego R35085-5) and focused using a widefield lens ($f = 400$ mm) to the back aperture of the objective lens (Nikon S Plan Fluor ELWD 20x, NA = 0.45). The photoluminescence (PL) from the sample is separated from the excitation light with a dichroic beam splitter (DBS) and a 550 nm longpass filter. The PL is either sent to a spectrometer (Ocean Insight Maya2000-Pro) or imaged with a scientific CMOS camera (Andor Zyla 5.5-W USB3) using a $f = 300$ mm tube lens. When imaging, additional shortpass and longpass optical filters were inserted to only collect a given wavelength range. A simplified schematic of the setup is shown in Supplementary Fig. 1 to emphasise that only the PL emission filters are changed when measuring the V_B^- or C_7 defects. The laser spot diameter ($1/e^2$) at the sample was about $50 \mu\text{m}$ and the total CW laser power up to 500 mW, which gives a maximum intensity of about $0.5 \text{ mW}/\mu\text{m}^2$ in the centre of the spot. For Fig. 4, the laser power at the sample was reduced to 25 mW to minimise laser-induced heating.

Radiofrequency (RF) driving was provided by a signal generator (Windfreak SynthNV PRO) gated using an IQ modulator (Texas

Instruments TRF37T05EVM) and amplified (Mini-Circuits HPA-50W-63+). A pulse pattern generator (SpinCore PulseBlasterESR-PRO 500 MHz) was used to gate the excitation laser and RF, as well as for triggering the camera. The output of the amplifier was connected to a printed circuit board (PCB) equipped with a coplanar waveguide and terminated by a 50Ω termination. The hBN sample was placed above the coplanar waveguide, either in direct contact (Figs. 1–3) or on a quartz coverslip placed on the PCB (Fig. 4).

The external magnetic field was applied using a permanent magnet, and the measurements were performed at room temperature in ambient atmosphere. The only exception is Fig. 1e, for which the sample was placed in a closed-cycle cryostat with a base temperature of $T \approx 5 \text{ K}$ ⁴⁷ which allowed us to apply a calibrated magnetic field using the enclosed superconducting vector magnet.

Sample preparation

The hBN powders used in Fig. 1 and for the dual-spin-species imaging experiment (Supplementary Fig. 19) were sourced from Graphene Supermarket (BN Ultrafine Powder), with a specified purity of 99.0%. Two batches of powder nominally identical but purchased at different times were used: ‘Powder 1’ was purchased in 2022 whereas ‘Powder 2’ was purchased in 2017. The as-received powders were electron irradiated with a beam energy of 2 MeV and a variable dose between $1 \times 10^{18} \text{ cm}^{-2}$ and $5 \times 10^{18} \text{ cm}^{-2}$. No annealing or further processing was performed. The experiments reported in Fig. 1 used Powder 1 with a dose of $2 \times 10^{18} \text{ cm}^{-2}$, whereas the experiments reported in Supplementary Fig. 19 used Powder 2 with a dose of $1 \times 10^{18} \text{ cm}^{-2}$. To form thin films of the hBN powders, the powder was suspended in isopropyl alcohol (IPA) at a concentration of 20 mg/mL and sonicated for 30 min using a horn-sonicator. The sediment from the suspension was drawn using a pipette then drop-cast on a glass coverslip or directly onto the PCB, generally forming a relatively continuous film. Morphological,

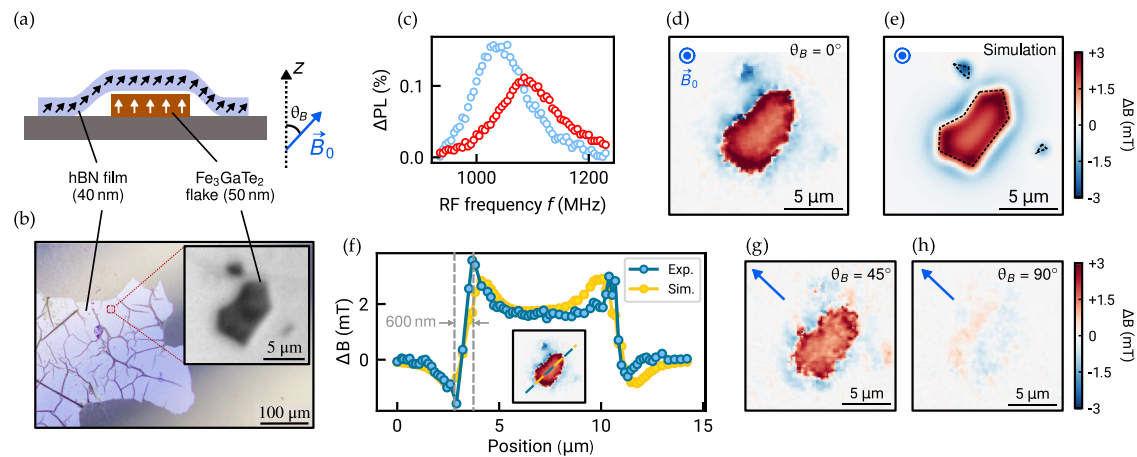


Fig. 4 | Magnetic imaging with $S = 1/2$ defects in hBN. **a** Schematic of the experiment. A 40-nm-thick hBN film containing C_7 spins (black arrows) is placed on top of a Fe_3GaTe_2 flake exhibiting perpendicular magnetic anisotropy (white arrows). The external field \vec{B}_0 sets the quantisation axis of the C_7 spins. **b** Optical micrograph of the hBN film covering multiple Fe_3GaTe_2 flakes. Inset: magnified view of the Fe_3GaTe_2 flake studied in (c–h). **c** ODMR spectra taken at the centre of the flake (red data) and outside the flake (black), with $B_0 \approx 35$ mT pointing along the z direction ($\theta_B = 0^\circ$). The dashed lines are Lorentzian fits. **d** Stray magnetic field

image of a Fe_3GaTe_2 obtained with the C_7 defects at room temperature. **e** Simulated stray field for a uniformly magnetised flake (see details in Supplementary Note 7 C). **f** Line profile of the measured and simulated stray field across the flake, taken along the dashed line displayed in (e). **g, h** Stray field images obtained with the same applied field magnitude $B_0 \approx 35$ mT as in (d) but with an angle (g) $\theta_B = 45^\circ$ and (h) $\theta_B = 90^\circ$. The blue arrow in (g, h) indicates the direction of the in-plane component of \vec{B}_0 .

optical, and spin characterisations of the powder films are presented in Supplementary Note 2.

The hBN single-crystal samples used in Fig. 2 and Fig. 3 were sourced from HQ Graphene, and had a thickness of $\sim 100 \mu\text{m}$ and a lateral size of ~ 1 mm. The as-received crystals were electron irradiated with a beam energy of 2 MeV and a dose between $2 \times 10^{18} \text{ cm}^{-2}$ and $1 \times 10^{19} \text{ cm}^{-2}$. No annealing or further processing was performed. In Fig. 3, a whole bulk crystal was placed on the PCB and measured. In Fig. 2, a thinner flake ($\sim 1 \mu\text{m}$) was exfoliated from a bulk crystal using scotch-tape and transferred to the PCB. Exfoliation of a thin flake allowed us to achieve a stronger and more uniform RF driving compared to using the whole crystal. Optical and spin characterisations are presented in Supplementary Note 3.

The hBN film used in Fig. 4 was grown by metal-organic vapour-phase epitaxy (MOVPE) on a 2-inch sapphire wafer, using precursors triethylboron (TEB) and ammonia. The growth details can be found in ref. 40. The film used in our work was grown with a TEB flow of 30 $\mu\text{mol}/\text{min}$, and has a thickness of about 40 nm determined by atomic force microscopy. In ref. 21, it was shown that this TEB flow leads to a dense and uniform ensemble of carbon-related optical emitters, including the ODMR-active C_7 defects studied in this paper. Optical and spin characterisations are presented in Supplementary Note 4. For the magnetic imaging experiment reported in Fig. 4, as a test magnetic sample we used a Fe_3GaTe_2 crystal purchased from PrMat. Fe_3GaTe_2 microflakes were first exfoliated in an Argon-filled glove box onto a Si/SiO₂ substrate using the scotch-tape technique. Then, the hBN film and Fe_3GaTe_2 flakes were picked up in sequence by a polycarbonate/polydimethylsiloxane (PC/PDMS) stamp and released onto a quartz substrate. Finally, the PC film was dissolved with chloroform. The quartz substrate was then positioned above a coplanar waveguide to facilitate ODMR measurements. A Fe_3GaTe_2 flake was located from the reflection image, and then via the PL image where the flake typically appears brighter than the background because it reflects additional PL from the C_7 defects. Images of the sample throughout the process are shown in Supplementary Note 7.

Data availability

The data supporting the findings of this study are available within the paper and its supplementary information files.

References

- Gottscholl, A. et al. Initialization and read-out of intrinsic spin defects in a van der Waals crystal at room temperature. *Nat. Mater.* **19**, 540–545 (2020).
- Liu, W. et al. Spin-active defects in hexagonal boron nitride. *Mater. Quantum Technol.* **2**, 032002 (2022).
- Aharonovich, I., Tetienne, J.-P. & Toth, M. Quantum emitters in hexagonal boron nitride. *Nano Lett.* **22**, 9227–9235 (2022).
- Vaidya, S., Gao, X., Dikshit, S., Aharonovich, I. & Li, T. Quantum sensing and imaging with spin defects in hexagonal boron nitride. *Adv. Phys.: X* **8**, 2206049 (2023).
- Durand, A. et al. Optically active spin defects in few-layer thick hexagonal boron nitride. *Phys. Rev. Lett.* **131**, 116902 (2023).
- Yao, N. Y., Zaletel, M. P., Stamper-Kurn, D. M. & Vishwanath, A. A quantum dipolar spin liquid. *Nat. Phys.* **14**, 405–410 (2018).
- Davis, E. J. et al. Probing many-body dynamics in a two-dimensional dipolar spin ensemble. *Nat. Phys.* **19**, 836–844 (2023).
- Choi, J.-y et al. Exploring the many-body localization transition in two dimensions. *Science* **352**, 1547–1552 (2016).
- Choi, S. et al. Observation of discrete time-crystalline order in a disordered dipolar many-body system. *Nature* **543**, 221–225 (2017).
- Abanin, D. A., Altman, E., Bloch, I. & Serbyn, M. Colloquium: many-body localization, thermalization, and entanglement. *Rev. Mod. Phys.* **91**, 021001 (2019).
- Zu, C. et al. Emergent hydrodynamics in a strongly interacting dipolar spin ensemble. *Nature* **597**, 45–50 (2021).
- Gong, R. et al. Coherent dynamics of strongly interacting electronic spin defects in hexagonal boron nitride. *Nat. Commun.* **14**, 3299 (2023).
- Gottscholl, A. et al. Spin defects in hBN as promising temperature, pressure and magnetic field quantum sensors. *Nat. Commun.* **12**, 4480 (2021).
- Liu, W. et al. Temperature-dependent energy-level shifts of spin defects in hexagonal boron nitride. *ACS Photonics* **8**, 1889–1895 (2021).
- Healey, A. J. et al. Quantum microscopy with van der Waals heterostructures. *Nat. Phys.* **19**, 87–91 (2023).
- Huang, M. et al. Wide field imaging of van der Waals ferromagnet Fe_3GeTe_2 by spin defects in hexagonal boron nitride. *Nat. Commun.* **13**, 5369 (2022).

17. Lyu, X. et al. Strain quantum sensing with spin defects in hexagonal boron nitride. *Nano Lett.* **22**, 6553–6559 (2022).
18. Kumar, P. et al. Magnetic imaging with spin defects in hexagonal boron nitride. *Phys. Rev. Appl.* **18**, L061002 (2022).
19. Robertson, I. O. et al. Detection of paramagnetic spins with an ultrathin van der Waals quantum sensor. *ACS Nano* **17**, 13408–13417 (2023).
20. Gao, X. et al. Quantum sensing of paramagnetic spins in liquids with spin qubits in hexagonal boron nitride. *ACS Photonics* **10**, 2894–2900 (2023).
21. Mendelson, N. et al. Identifying carbon as the source of visible single-photon emission from hexagonal boron nitride. *Nat. Mater.* **20**, 321–328 (2021).
22. Chejanovsky, N. et al. Single-spin resonance in a van der Waals embedded paramagnetic defect. *Nat. Mater.* **20**, 1079–1084 (2021).
23. Stern, H. L. et al. Room-temperature optically detected magnetic resonance of single defects in hexagonal boron nitride. *Nat. Commun.* **13**, 618 (2022).
24. Guo, N.-J. et al. Coherent control of an ultrabright single spin in hexagonal boron nitride at room temperature. *Nat. Commun.* **14**, 2893 (2023).
25. Yang, Y.-Z. et al. Laser direct writing of visible spin defects in hexagonal boron nitride for applications in spin-based technologies. *ACS Appl. Nano Mater.* **6**, 6407–6414 (2023).
26. Auburger, P. & Gali, A. Towards ab initio identification of paramagnetic substitutional carbon defects in hexagonal boron nitride acting as quantum bits. *Phys. Rev. B* **104**, 075410 (2021).
27. Jara, C. et al. First-principles identification of single photon emitters based on carbon clusters in hexagonal boron nitride. *J. Phys. Chem. A* **125**, 1325–1335 (2021).
28. Golami, O. et al. Ab initio and group theoretical study of properties of a carbon trimer defect in hexagonal boron nitride. *Phys. Rev. B* **105**, 184101 (2022).
29. Li, K., Smart, T. J. & Ping, Y. Carbon trimer as a 2 eV single-photon emitter candidate in hexagonal boron nitride: a first-principles study. *Phys. Rev. Mater.* **6**, L042201 (2022).
30. McCamey, D. R. et al. Hyperfine-field-mediated spin beating in electrostatically bound charge carrier pairs. *Phys. Rev. Lett.* **104**, 017601 (2010).
31. Davies, J. Optically-detected magnetic resonance studies of ii-vi compounds. *J. Cryst. Growth* **86**, 599–608 (1988).
32. Boehme, C. & Lips, K. Theory of time-domain measurement of spin-dependent recombination with pulsed electrically detected magnetic resonance. *Phys. Rev. B* **68**, 245105 (2003).
33. McCamey, D. et al. Spin rabi flopping in the photocurrent of a polymer light-emitting diode. *Nat. Mater.* **7**, 723–728 (2008).
34. Hall, L. T. et al. Detection of nanoscale electron spin resonance spectra demonstrated using nitrogen-vacancy centre probes in diamond. *Nat. Commun.* **7**, 10211 (2016).
35. Broadway, D. A. et al. Quantum probe hyperpolarisation of molecular nuclear spins. *Nat. Commun.* **9**, 1246 (2018).
36. Haykal, A. et al. Decoherence of V_B^- spin defects in monoisotopic hexagonal boron nitride. *Nat. Commun.* **13**, 1–7 (2022).
37. Baber, S. et al. Excited state spectroscopy of boron vacancy defects in hexagonal boron nitride using time-resolved optically detected magnetic resonance. *Nano Lett.* **22**, 461–467 (2022).
38. Fuchs, G., Burkard, G., Klimov, P. & Awschalom, D. A quantum memory intrinsic to single nitrogen-vacancy centres in diamond. *Nat. Phys.* **7**, 789–793 (2011).
39. Tetienne, J.-P. et al. Magnetic-field-dependent photodynamics of single NV defects in diamond: an application to qualitative all-optical magnetic imaging. *N. J. Phys.* **14**, 103033 (2012).
40. Chugh, D. et al. Flow modulation epitaxy of hexagonal boron nitride. *2D Mater.* **5**, 045018 (2018).
41. Zhang, G. et al. Above-room-temperature strong intrinsic ferromagnetism in 2d van der Waals Fe_3GaTe_2 with large perpendicular magnetic anisotropy. *Nat. Commun.* **13**, 5067 (2022).
42. Bedoya-Pinto, A. et al. Intrinsic 2d-xy ferromagnetism in a van der Waals monolayer. *Science* **374**, 616–620 (2021).
43. Huang, M. et al. Revealing intrinsic domains and fluctuations of moiré magnetism by a wide-field quantum microscope. *Nat. Commun.* **14**, 5259 (2023).
44. Rizzato, R. et al. Extending the coherence of spin defects in hbn enables advanced qubit control and quantum sensing. *Nat. Commun.* **14**, 5089 (2023).
45. Ramsay, A. J. et al. Coherence protection of spin qubits in hexagonal boron nitride. *Nat. Commun.* **14**, 461 (2023).
46. Wolfowicz, G. et al. Quantum guidelines for solid-state spin defects. *Nat. Rev. Mater.* **6**, 906–925 (2021).
47. Lillie, S. E. et al. Laser modulation of superconductivity in a cryogenic wide-field nitrogen-vacancy microscope. *Nano Lett.* **20**, 1855–1861 (2020).

Acknowledgements

This work was supported by the Australian Research Council (ARC) through grants CE170100012, CE170100039, CE200100010, FT200100073, FT220100053, DE200100279, DE230100192, and DP220100178, and by the Office of Naval Research Global (N62909-22-1-2028). The work was performed in part at the RMIT Micro Nano Research Facility (MNRFF) in the Victorian Node of the Australian National Fabrication Facility (ANFF). The authors acknowledge the facilities, and the scientific and technical assistance of the RMIT Microscopy & Microanalysis Facility (RMMF), a linked laboratory of Microscopy Australia, enabled by NCRIS. We thank Hoe Tan from the Australian National University for providing the MOVPE films. S.C.S. gratefully acknowledges the support of an Ernst and Grace Matthaehi scholarship. I.O.R. is supported by an Australian Government Research Training Program Scholarship. G.H. is supported by the University of Melbourne through a Melbourne Research Scholarship. P.R. acknowledges support through an RMIT University Vice-Chancellor's Research Fellowship. Part of this study was supported by QST President's Strategic Grant "QST International Research Initiative".

Author contributions

J.-P.T. and I.A. conceived and supervised the research. S.C.S. and P.S. performed the experiments and data analysis, with assistance and inputs from A.J.H., I.O.R., G.H., D.A.B., M.K., and P.R. C.T. fabricated the hBN/ Fe_3GaTe_2 device, with inputs from L.W. H.A., and T.O. performed the electron irradiation. S.C.S., P.S., I.A., and J.-P.T. wrote the manuscript, with inputs from all authors.

Competing interests

The authors declare no competing interests.

Additional information

Supplementary information The online version contains supplementary material available at <https://doi.org/10.1038/s41467-024-51129-8>.

Correspondence and requests for materials should be addressed to Igor Aharonovich or Jean-Philippe Tetienne.

Peer review information *Nature Communications* thanks the anonymous reviewers for their contribution to the peer review of this work.

Reprints and permissions information is available at <http://www.nature.com/reprints>

Publisher's note Springer Nature remains neutral with regard to jurisdictional claims in published maps and institutional affiliations.

Open Access This article is licensed under a Creative Commons Attribution-NonCommercial-NoDerivatives 4.0 International License, which permits any non-commercial use, sharing, distribution and reproduction in any medium or format, as long as you give appropriate credit to the original author(s) and the source, provide a link to the Creative Commons licence, and indicate if you modified the licensed material. You do not have permission under this licence to share adapted material derived from this article or parts of it. The images or other third party material in this article are included in the article's Creative Commons licence, unless indicated otherwise in a credit line to the material. If material is not included in the article's Creative Commons licence and your intended use is not permitted by statutory regulation or exceeds the permitted use, you will need to obtain permission directly from the copyright holder. To view a copy of this licence, visit <http://creativecommons.org/licenses/by-nc-nd/4.0/>.

© The Author(s) 2024